Petrologic imaging of the magma reservoirs that feed large silicic eruptions

Etienne Médard, Jean-Luc Le Pennec

Petrologic imaging of the magma reservoirs that feed large silicic eruptions

Etienne Médard[1], Jean-Luc Le Pennec[2,3]

[1]*Université Clermont Auvergne, CNRS, IRD, OPGC, Laboratoire Magmas et Volcans, F-63000 Clermont-Ferrand, France*

[2]*Geo-Ocean, CNRS, Ifremer, UMR6538, F-29280 Plouzané, France*

[3]*IRD Office for Indonesia & Timor Leste, Jalan Kemang Raya n°4, Jakarta 12730, Indonesia*

ABSTRACT

Large silicic explosive eruptions are one of Nature's most hazardous phenomena. Very few have been witnessed and unravelling the complex conditions that lead to these eruptions remains a difficult task because the characteristics of the feeding magma reservoirs are still insufficiently constrained from geophysical imaging. Here we show that a barometer based on the composition of amphibole in equilibrium with plagioclase and biotite, common minerals in the eruptive products of large silicic eruptions, records the thickness and depth of magma reservoirs with uncertainties of 0.8 and 2.7 km, respectively. Pressures are given by the equation: P (MPa) = 892 · ^{VI}Al + 101, where ^{VI}Al is the octahedral aluminum content of the amphibole. With the example of a Miocene Turkish ignimbrite, we show that reservoirs feeding large silicic eruptions can be pancake-shaped. Our new barometer, valid between 650 and 950 °C, can be used in combination with volcanological and geophysical data to infer the size, shape and depth of magma reservoirs and may serve as a tool for monitoring future activity. This temperature-independent barometer is also applicable to any volcanic or plutonic rock containing amphibole + plagioclase + biotite and is in excellent agreement with previously published temperature-dependent barometers within their calibration range.

1. Introduction

Large silicic eruptions can bury large areas (thousands of km^2) beneath thick tephra covers around their source (e.g., Miller and Wark, 2008) and may have a pronounced

impact on global atmospheric circulation and climate (e.g., Self and Blake, 2008). None has been observed in detail by volcanologists, but geophysical monitoring signals suggest new large silicic eruptions could occur in the geologically near-future (e.g., Laguna del Maule in Chile, Le Mével et al., 2016; Campi Flegrei in Italy, Kilburn et al., 2017; Long Valley and Yellowstone in the USA, Lowenstern et al., 2006; Seccia et al., 2011; Taupo in New Zealand, Heise et al., 2010), thus prompting scientists to better understand how these eruptions get prepared at depth. Geophysical signals resulting from magma motion in the crust are often used to monitor unrest and warn of upcoming eruptions. However, there is little information on reservoirs' characteristics and precursor signals of large silicic eruptions. For instance, the largest closely monitored eruption, the 1991 VEI 6 eruption of Mt Pinatubo, only erupted ~10 km^3 of magma (Newhall and Punongbayan, 1996). Larger eruptions with erupted bulk volumes of 100's km^3 are common in the geological record (Miller and Wark, 2008), but we lack constraints on the behavior of large silicic feeding system to uniquely interpret the geophysical information (Lowenstern et al., 2006; Pritchard and Gregg, 2016). The depth and shape of magmatic reservoirs can be investigated through mineral-based barometry (Putirka, 2008), with the most accurate models relying on the composition of amphibole, a common mineral in pyroclastic rocks from large silicic eruptions (e.g., Johnson and Rutherford, 1989). Here we present a new amphibole barometer that yields accurate results of reservoir depth and shape, with further constraints on size when combined with tephra/magma volume estimates.

Al-in amphibole barometry relates the aluminum content of amphibole crystals to their pressure of crystallization that correlates directly to crystallization depth. The barometric potential of the Al concentration in amphibole was first identified by comparing

amphibole compositions in plutonic intrusives to pressure derived from thermobarometric study of their metamorphic contact aureoles (Hammarstrom and Zen, 1986; Hollister et al., 1987), before being calibrated experimentally (Johnson and Rutherford, 1989; Schmidt, 1992). Calibrations are, in theory, only applicable to rocks containing the equilibrium assemblage amphibole + biotite + quartz + plagioclase + sanidine + magnetite + titanite or ilmenite. However, the absence of some of these phases results only in small additional uncertainties, and any silicic magmatic system containing equilibrium amphibole + biotite + plagioclase, and reasonably close to saturation with quartz and sanidine, can be constrained by amphibole barometry (Johnson and Rutherford, 1989).

Amphiboles are silicate minerals with a large range of possible substitutions (Hawthorne et al., 2012). The simplest formula is that of tremolite, $\square Ca_2{}^{VI}Mg_5{}^{IV}Si_8O_{22}(OH)_2$. It contains no trivalent cation thus aluminum (Al^{3+}) can only be incorporated through heterovalent substitutions, either in the octahedrally coordinated (^{VI}) site or the tetrahedrally coordinated (^{IV}) site. Three major substitutions have been described in calc-alkaline silicic rocks:

(1) the tschermak substitution: $^{VI}Mg + {}^{IV}Si = {}^{VI}Al + {}^{IV}Al$

(2) the edenite substitution: $\square + {}^{IV}Si = Na + {}^{IV}Al$

(3) the Ti-tschermak substitution: $^{VI}Mg + 2{}^{IV}Si = {}^{VI}Ti + 2{}^{IV}Al$

The tschermak substitution is pressure-dependent (Schmidt, 1992), whereas the edenite and Ti-tschermak substitutions are temperature-dependent (Bachmann and Dungan, 2002; Holland and Blundy, 1994), so the variations in total Al are controlled by both pressure and temperature. Barometers based on total Al in amphibole are thus only valid when temperature is fixed - either on an isotherm (Johnson and Rutherford, 1989) or along the

granite solidus (Schmidt, 1992). However, the pressure-dependent tschermak substitution is the only one to involve substitution of aluminum in the octahedral sites of the amphibole structure. By calculating structural formulae, the tschermak substitution can be dissociated from other substitutions by considering only octahedral aluminum ^{VI}Al, allowing for the construction of a temperature-independent barometer. Schmidt (1992) noticed the excellent correlation between ^{VI}Al and pressure, and attributed it to the tschermak substitution, but preferred to use total Al for his calibration. Two attempts have been made at calibrating a barometer based on ^{VI}Al versus pressure (Larocque and Canil 2010, Krawczynski et al. 2012) but are restricted to high-Mg rocks and have not gained wide acceptance in the community.

In this paper, we use published analyses of experimental amphiboles to calibrate a new temperature-independent amphibole-barometer based on the octahedral aluminum content. Combination of this new barometer with volume estimate for an ignimbritic eruption allow to constrain the depth and shape of a large silicic magma reservoir. We show that this method is a priori applicable to other large silicic systems and may be combined with possible geophysical precursor signals at potentially reactivating silicic volcanoes to better constrain their pre-eruptive evolution.

2. Methods

2.1. Barometer calibration database

A total of 47 amphibole compositions from experiments on rhyolitic and dacitic bulk compositions were compiled from the literature (Johnson and Rutherford, 1989; Mutch et al., 2016; Rutter et al., 1989; Schmidt, 1992; Thomas and Ernst, 1990; Supplementary Data

105 1). All amphiboles are in equilibrium with biotite, plagioclase, magnetite and a rhyolitic
106 silicate melt. Most amphiboles are in equilibrium with quartz and sanidine. We also
107 included a few experiments that did not contain quartz and/or sanidine, but in which the
108 silicate melt is SiO_2- (> 75 wt%) and K_2O- (> 5 wt%) rich, indicating that it is close to
109 saturation with both minerals. Four amphibole compositions were excluded from the
110 database because they showed large deviations from compositional trends. The first was
111 extracted from a set of reversal experiments (Thomas and Ernst, 1990). The excluded
112 reversal composition differs strongly from the corresponding forward experiment and does
113 not plot on the linear trend defined by all other experiments. In two piston-cylinder
114 experiments from the most recent study (Mutch et al., 2016), ^{VI}Al concentrations in
115 amphibole are half the concentrations analysed in all other studies at similar pressures
116 (Johnson and Rutherford, 1989; Rutter et al., 1989; Schmidt, 1992; Thomas and Ernst,
117 1990). Amphibole crystals in these experiments are zoned (Mutch et al., 2016), a possible
118 indication that equilibrium has not been reached. For consistency, we discarded all three
119 piston-cylinder experiments from this study. The final dataset comprises 43 amphibole
120 compositions and covers a pressure range of 80 to 1,300 MPa, and experimental
121 temperatures from 650 to 850 °C, with oxygen fugacities mostly constrained near the NNO
122 buffer (Supplementary Data 1).
123
124 *2.2. Samples and sample preparation*
125 Three pumice samples were collected from the Kızılkaya ignimbrite, in the
126 Cappadocia area of Central Turkey. Sample KZ-041010-4a (UTM zone 36S; X = 671344;
127 Y = 4234915; Z = 1380 m) is from the Plinian fall deposit exposed below the main

ignimbrite sheet. Samples KZ-021010-1 (UTM zone 36S; X = 589770; Y = 4225687; Z = 1068 m) and KZ-021010-2 (UTM zone 36S; X = 588204; Y = 4220509; Z = 1102 m) are from different levels of the main flow unit of the ignimbrite. Each sample was crushed and sieved, and heavy minerals were separated into fractions using a Wilfley table, a magnetic separator, and heavy liquids. Euhedral amphibole and plagioclase crystals were then hand-picked, mounted in epoxy and polished. Samples of pumice from the three sites were also mounted in epoxy resin and polished. A large pumice sample was collected from the Paipatja pyroclastic density current deposit unit of the most recent (218 ± 14 ^{14}C years BP) eruption of Tutupaca volcano in Peru (UTM zone 19K; X = 362215; Y = 8119045; Z = 4680 m; Manrique et al., 2020; Samaniego et al., 2015). A zoned amphibole crystal and a neighbouring zoned plagioclase crystal were extracted from the pumice and mounted in Epoxy.

2.3. Electron microprobe analyses

Amphibole and plagioclase crystals were analysed using a SX-100 electron microprobe at Laboratoire Magmas et Volcans (Université Clermont Auvergne, Clermont-Ferrand, France), using a 15 kV acceleration voltage, a 40 nA beam current, and 5 µm diameter beam. The beam current is higher than commonly used for major element analyses, with the goal of reducing analytical uncertainties and thus improving the precision of pressure estimates. We analysed a total of 188 amphibole phenocrysts rims from the three samples of the Kızılkaya ignimbrite, as well as plagioclase rims from the same samples (Supplementary Data 2). Standards used for calibration include natural wollastonite (Si, Ca), orthoclase (Al, K), and albite (Na), and synthetic $TiMnO_3$ (Ti, Mn),

fayalite (Fe), forsterite (Mg), and Cr_2O_3 (Cr). All investigated phenocrysts show euhedral shapes and are homogeneous, i.e., with no significant zoning. Amphibole and plagioclase compositions from the Tutupaca sample were analysed with the same procedure. We also analysed glasses from pumices of the Kızılkaya ignimbrite, using an enlarged beam size (20 μm diameter), and decreased beam current (5 nA) to avoid Na-loss. We used the same standards than for mineral analyses, with the addition of natural fluorapatite for P. Analytical results, analytical uncertainties, calculated structural formulae, and calculated pressures are presented in Supplementary Data 2.

2.4. Raman spectrometry

Water concentrations were analysed by Raman spectroscopy in a series of melt inclusions trapped in amphibole crystals from the Kızılkaya ignimbrite. These measurements are then used to calculate volatile-saturation pressures and compare them with mineral barometry. Raman spectra were collected using a Renishaw InVia confocal Raman micro-spectrometer with a 532 nm wavelength. Detailed analytical conditions are presented in Schiavi et al. (2018). Reference glasses used for calibration include a series of in-house rhyolitic glasses. We used an internal calibration based on the correlation between water content and the area ratio of the water band and the alumino-silicate band (Schiavi et al., 2018).

2.5. Amphibole-plagioclase thermometry

Pre-eruptive temperatures for the Kızılkaya ignimbrite were estimated using amphibole-plagioclase thermometry. All three samples contain quartz phenocrysts, so we

174 can use thermometry based on the equilibrium edenite + quartz = tremolite + albite
175 (Holland and Blundy, 1994). Amphibole and plagioclase rims from the Kızılkaya
176 ignimbrite equilibrated at 728 ± 13 °C.
177
178 **3. Results: temperature-independent amphibole barometer**
179 *3.1. Barometer calibration*
180 We calculated structural formulae from published experimental amphibole
181 compositions in equilibrium with biotite, plagioclase, magnetite, quartz and sanidine at
182 650-850 °C (Supplementary Data 1). Correlations between total Al and pressure and
183 between octahedral Al and pressure are presented in Figure 1. Correlations between total Al
184 and pressure are usually excellent within a given dataset (R^2 = 0.99, Johnson and
185 Rutherford 1989; Schmidt 1992, Figure 1a). However, these datasets were acquired over a
186 restricted temperature range (750-780 °C for Johnson and Rutherford 1989, 655-700 °C for
187 Schmidt 1992). When comparing datasets at different temperatures, the offset between
188 calibrations becomes significant (145 MPa between the calibrations of Johnson and
189 Rutherford 1989 and Schmidt 1992), confirming that total Al depends not only on pressure
190 but also on temperature, and that calibrations based on total Al can only be used at
191 temperatures close to their calibration temperatures. Individual correlations are usually
192 linear, except for the very-low pressure set of data (≤ 200 MPa) published by Mutch et al.
193 (2016) which shows some non-linearity. This non-linearity is, however, purely due to ^{IV}Al
194 and is not visible in the ^{VI}Al versus pressure plot (Figure 1b), thus is likely due to
195 temperature effects.

196 ^{VI}Al shows a very good linear correlation with pressure, independently of
197 experimental temperature (R^2 = 0.939, Figure 1b):
198
199 $$P\ (MPa) = 892 \cdot {}^{VI}Al + 101 \quad (1)$$
200
201 For the entire calibration range, the standard error of estimate (SEE = square root of
202 average squared value of the difference between calculated and experimental pressures),
203 i.e., the accuracy of the barometer, is 86 MPa (Supplementary Data 1).
204
205 *3.2. Precision and accuracy*
206 Pressure estimates are affected by calibration and analytical uncertainties. Analytical
207 uncertainties control the precision of the pressure estimate. For barometers relying solely
208 on the aluminum content of the amphibole, those uncertainties are negligible (around 8
209 MPa) and only depend on the precision of aluminum measurements. Since our new
210 barometer uses octahedral aluminum, other elements have an influence on structural
211 formula calculations, resulting in a lower precision. We propagated analytical errors using a
212 Monte-Carlo approach, by randomly generating a thousand synthetic analyses following a
213 gaussian distribution around the measured value for each analyzed element, computing the
214 resulting pressure for each of the thousand analyses, and calculating the resulting standard
215 deviation. Regular analytical conditions used in our lab (15 kV, 15 nA, 10 s counting time)
216 produce a 2σ precision of 36 MPa. This value can be decreased to at least 20 MPa by
217 increasing beam current and counting time (Figure 2). Most of the analyses presented in
218 this paper were performed using a 40 nA beam current and a 30 s counting time, resulting
219 in a 21 MPa precision (at the 2σ level). For magmatic systems of rhyolitic to dacitic

compositions located in the upper crust, and assuming a granitic crust with a density of 2700 $kg \cdot m^{-3}$, the depth precision of our barometer is thus 0.8 km.

Calibration uncertainties control the accuracy of the barometer. We estimated the standard error of estimate of our barometer using the 43 experimental amphiboles used for the calibration. The standard error of estimate (SEE), i.e., the accuracy of the barometer, for the entire dataset is 86 MPa. The main silicic reservoirs feeding super-volcanoes are, however, located in the upper crust (depth ≤ 15 km, Bachmann and Bergantz, 2008, Huber et al. 2019). Within the corresponding pressure range (≤ 400 MPa), the experimental pressures are reproduced with an improved accuracy of 72 MPa. For upper crustal magmatic systems of rhyolitic to dacitic compositions, assuming a crustal density of 2700 $kg \cdot m^{-3}$, the depth accuracy of the barometer is thus 2.7 km. This accuracy is slightly higher than that reported for previous barometers based on total aluminum (50 MPa, Johnson and Rutherford 1989; 60 MPa, Schmidt et al. 1992; 50 MPa, Mutch et al. 2016). However, when comparing to our entire database, and not only each author's calibration database, the barometers are less accurate i.e. the SEE is higher: 133 MPa for Johnson and Rutherford (1989), 125 MPa for Schmidt (1992), 96 MPa for Mutch et al. 2016).

3.3. Influence of temperature

We tested the validity of our new barometer by analyzing a zoned amphibole crystal from the most recent eruption of Tutupaca volcano in Peru (Samaniego et al., 2015). The host rock is a dacitic pumice with phenocrysts of plagioclase, amphibole, biotite, clinopyroxene, titanite, magnetite, apatite and quartz. The investigated amphibole crystal records a sharp increase in temperature from 750 °C in the core to 950 °C in the rim

(Manrique et al., 2020, Figure 3, Supplementary Data 2), indicating that the magma reservoir was re-heated before crystallization of the mineral rims.

Crystallization pressures predicted for the core of the investigated amphibole crystal by previously published Al-in amphibole barometers (Johnson and Rutherford, 1989; Mutch et al., 2016; Ridolfi et al., 2010; Ridolfi and Renzulli, 2012; Rutter et al., 1989; Thomas and Ernst, 1990) varies from 126 to 386 MPa (Figure 3). These pressures are directly correlated to the temperature at which the barometer was calibrated (Figure 4), further highlighting the influence of temperature on aluminum concentration in amphibole. Barometers based on total aluminum concentration in amphiboles can thus only be used if the temperature is close to their average calibration temperature. All these barometers also predict a 120-256 MPa increase in pressure from core to rim, equivalent to a 4.5-9.7 km increase in depth (Figure 3). Such an increase is physically highly unlikely, and previous studies on similar material have shown that it is an artefact because these barometers do not differentiate the influence of temperature and pressure on aluminum concentration (Bachmann and Dungan, 2002; Rutherford and Devine, 2003; Shane and Smith, 2013). Although only one profile is reported in this paper, core ("high-Al") + rim ("low-Al") analyses have been performed on a large number of amphibole crystals from the same eruption by Manrique et al. (2020). Data reported in their Table 7 for all crystals confirm the results presented here, with a 120-270 MPa "pressure" increase between core and rim calculated by barometers relying on total Al, and only a 23 MPa difference recorder by our new barometer, well within uncertainties. Although amphibole-barometry is an extremely powerful tool, total aluminum concentrations should only be used after a thorough

265 investigation of crystal chemistry variations and with a good estimate of crystallization
266 temperatures.

267 In the investigated crystal, the Al variation can be fully explained by temperature-
268 dependent variations in ^{IV}Al through edenite and Ti-tschermak substitutions. Our new
269 barometer produces no pressure variation throughout the amphibole crystal (Figure 3),
270 despite the 200 °C temperature increase, evidencing that it is independent of temperature.
271 Calculated core pressure (crystallization temperature 750 °C) is in excellent agreement with
272 that calculated using a calibration based on total aluminum performed at an average
273 temperature of 760 °C (Johnson and Rutherford, 1989). At high temperatures (950 °C for
274 the rim), our model is consistent with a model calibrated on dacitic to basaltic rocks
275 (Ridolfi and Renzulli, 2012) at an average temperature of 936 °C, despite using a different
276 calibration database with no common data points (rhyolites to dacites at 650-850 °C vs
277 dacites to basalts at 800-1130 °C). These results suggest that our model can be extrapolated
278 to higher temperatures beyond its calibration range. To demonstrate its applicability at
279 higher temperature, we tested our model against a recent independent set of experimental
280 amphibole compositions in equilibrium with plagioclase and biotite at 900-950 °C (8
281 datapoints from Rondet et al., 2019). Experimental pressures are reproduced with an
282 excellent SEE of 41 MPa (Figure 5).

283 Since biotite is less common in silicic rocks than amphibole and plagioclase, we
284 tested the applicability of our barometer to biotite-free rocks using a recent series of
285 experiments on a biotite-free dacite from Quizapu, Chile (First et al. 2021). We selected
286 fourteen experiments for which at least five different amphibole analyses were reported.
287 These experiments were run between 75-175 MPa and 810-890 °C and contain both

amphibole and plagioclase, half of them biotite-free, half of them containing biotite. Our new barometer reproduces experimental pressure with an SEE of 74 MPa for biotite-bearing experiments (Figure 5, similar to the 72 MPa SEE of the calibration database). However, for biotite-free experiments, the calculated pressure is on average 146 MPa higher than experimental pressure (SEE of 144 MPa). Although this is only one example, and amphibole-barometry in biotite-free rocks requires further investigation, we do not recommend using our new barometer on biotite-free rocks, since this may result in overestimated calculated pressures.

3.4. Influence of oxygen fugacity

The distribution of aluminum between tetrahedral and octahedral sites is sensitive to the way structural formulae are calculated, and in particular the proportions of ferric and ferrous iron. Most amphibole crystals in our experimental database have either been synthesized under controlled oxygen fugacity buffered by a mix of Ni and NiO (NNO buffer; Schmidt, 1992, and part of the data from Johnson and Rutherford, 1989) or under conditions demonstrated to be close to those of the NNO buffer (Mutch et al., 2016; Rutter et al., 1989; Thomas and Ernst, 1990). According to Clowe et al. (1988), calcic amphiboles equilibrated near the NNO buffer have $Fe^{3+}/\Sigma Fe \sim 0.2$. The structural formula of experimental amphiboles in the calibration database was thus calculated based on 46 charges (23 oxygens) and assuming 20% of iron is ferric (Clowe et al., 1988), unless the sum of cations excluding Na^+ and K^+ exceeds 15. In that latter case, the ratio $Fe^{3+}/\Sigma Fe$ is increased to satisfy stoichiometry criteria (Supplementary Data 1). This was only required for one amphibole composition where $Fe^{3+}/\Sigma Fe$ was increased to 0.36. Varying the

311 $Fe^{3+}/\Sigma Fe$ ratio from 0.1 to 0.3 (Clowe et al., 1988; Schmidt, 1992) does not significantly
312 change the results: it produces parallel calibrations, with pressure offsets of +30 MPa
313 ($Fe^{3+}/\Sigma Fe = 0.3$) to -25 MPa ($Fe^{3+}/\Sigma Fe = 0.1$), well within the barometer uncertainty. Some
314 of the experiments by Johnson and Rutherford (1989) are more oxidized (up to the MNO
315 buffer), however, there is no systematic variations in octahedral Al content with
316 experimental oxygen fugacity. Data from a recent study by Rondet et al. (2019) on
317 amphiboles in equilibrium with plagioclase and biotite at oxygen fugacities between
318 NNO+0.5 and NNO+2.1 also do not show any systematic variations in the predicted
319 pressure as a function of oxygen fugacity. For applications of our new amphibole
320 barometer, we thus recommend using the same procedure for structural formulae
321 calculation, with known $Fe^{3+}/\Sigma Fe$ when available. In the absence of independent constraints
322 on $Fe^{3+}/\Sigma Fe$, we recommend using a $Fe^{3+}/\Sigma Fe$ ratio of 0.2. If the investigated amphiboles
323 are more oxidized, the pressure will be slightly underestimated by this approach.
324
325 4. **Characterization of the magma reservoir that fed a large silicic eruption**
326 *4.1. The Kızılkaya ignimbrite in Turkey*
327 The Kızılkaya ignimbrite is the product of a large eruption in the Cappadocia area of
328 Central Turkey. This area superbly exposes a succession of Neogene dacitic to rhyolitic
329 ignimbrites and fallout deposits, recording 10 Ma of magmatic activity (Aydar, 2012; Le
330 Pennec et al., 1994; Viereck-Goette et al., 2010). The succession provides an excellent
331 example of a long-lived silicic system, with ignimbrite eruptions at mid-to-low frequency
332 in Mio-Pliocene times, and with a moderate average magma output rate (about 10^{-3} km^3/a),
333 but large silicic eruptions (bulk volumes exceeding 300 and 180 km^3 for Cemilköy and

Kızılkaya ignimbrite units, respectively). The Kızılkaya ignimbrite is U-Pb dated at 5.43 ± 0.06 Ma (Paquette and Le Pennec, 2012) and covers an area of more than 10 000 km^2. Juvenile pumice is rhyolitic (71-73 wt% SiO_2), with phenocrysts of plagioclase, biotite, amphibole, magnetite, ilmenite, quartz, apatite and zircon (Temel et al., 1998). No significant variation in mineral or glass composition was observed over the three investigated samples. For example, the SiO_2 content in the glass is 77.6 ± 0.4 (2σ), a variation within the analytical uncertainty of the electron microprobe.

4.2. Average depth of magma storage

A total of 188 amphibole phenocrysts were analyzed by electron microprobe to constrain pre-eruptive pressures and temperatures (Supplementary Data 2). All investigated crystals are euhedral and homogeneous. They are thus all juvenile phenocrysts, and amphibole xenocrysts and antecrysts, if present (Paquette and Le Pennec, 2012), were either not sampled, or dissolved prior to the eruption. Pre-eruptive temperature is 728 ± 13 °C, well within the calibration range of our new barometer (650-850 °C). The pressure distribution of all crystal rims (Figure 6a), calculated from their ^{VI}Al content, is close to Gaussian with an average value of 214 MPa and a standard deviation of 18 MPa. Assuming a crustal density of 2700 $kg \cdot m^{-3}$, the average depth of the magma chamber is 8.1 ± 2.7 km. This value is within the range of typical eruptible rhyolitic reservoirs, as shown by petrological and geophysical methods (Huber et al. 2019 and references therein). It is also in good agreement with thermo-mechanical models that show an optimal depth for eruptible large silicic reservoirs around 200 ± 50 MPa – at lower pressures, volatile exsolution hinders chamber growth whereas at higher pressure the low viscosity of the crust

inhibits eruption (Huber et al. 2019). We also analyzed water concentrations in primary rhyolitic melt inclusions trapped in amphibole crystals by Raman spectrometry (Table 1). The maximum H_2O concentration is 4.95 wt%, well within the "optimal" 4.0-5.5 wt. % H_2O concentration estimated by Poppa et al. (2021) to trigger explosive silicic eruptions. Assuming that the magma is saturated with a pure H_2O volatile phase, the storage pressure is estimated at 170 MPa (Papale et al., 2006), slightly lower but well within uncertainty of the pressure calculated by amphibole barometry (214 ± 72 MPa). If the saturating fluid phase contained small amount of CO_2, the entrapment pressure would be higher. Also, since the eruptible part of the magma body is likely slightly below fluid-saturation (e.g., Poppa et al. 2021), this saturation pressure is expected to be lower than the storage pressure. Volatile saturation and Al-in-amphibole barometry are thus in good agreement with each other.

	OH area		Si area			
crystal	raw	normalized	Raw	normalized	OH/Si	H_2O
KZ0210-a2	746743	519	1264272	1317	0.39	3.71
KZ0210-a7	903204	627	1242755	1295	0.48	4.52
KZ0210-a8	733016	509	1301905	1356	0.38	3.55
KZ0210-a9	590354	410	1284089	1338	0.31	2.93
KZ0210-a10	643556	447	1193751	1243	0.36	3.41
KZ0210-a11	906644	630	1165255	1214	0.52	4.83
KZ0210-a13	899845	625	1127344	1174	0.53	4.95

Table 1: H_2O concentrations in melt inclusions in amphiboles from sample KZ021010-1

4.3. Volume of erupted material

The bulk volume of the Kızılkaya ignimbrite has been estimated in a previous work to 180 km^3 (Le Pennec et al., 1994), and no refinements have been proposed since. In that

work, the authors reconstructed the approximate pre-erosion distribution of the ignimbrite by drawing the envelope of all known outcrops of the Kızılkaya unit (10 600 km²). The deposit shows a fairly constant thickness of 15-30 m on the Nevsehir Plateau, and local overthickening (up to 80 m) in valleys. The ignimbrite thins distally to 2-3 m, 120 km from the presumed source. To account for uneven welding intensity, these authors assigned a welding intensity at localities where the ignimbrite is exposed, which allowed recalculating the pre-(welding) compaction thickness to obtain a homogenous density of 1000 $kg \cdot m^{-3}$. The bulk volume of 180 km^3 obtained with this method is considered a minimum estimate because large fractions of the loose top of the ignimbrite were likely removed by erosion and underestimated in the calculation (this may represent 10 to 20 % of the total bulk volume of the ignimbrite, maybe more).

The volume of the tephra fall deposit was not estimated in previous studies, notably because the overlying ignimbrite incorporated a large amount of material from the underlying loose Plinian tephra fall layer. Thickness variations in the Kızılkaya fall layer are thus poorly correlated to distance from source and constructing a reliable isopach map proved difficult (Le Pennec et al., 1994). To obtain a minimum estimate of the tephra fall layer volume we selected the 30 cm isopach contour that, in our interpretation, is the most reliable non-eroded one (e.g. it is exposed nicely 44 km east of the source, along the main dispersal axis). The area inside the 30 cm isopach is about 691 km². Using a single isopach approximation approach (Legros, 2000), we thus estimate the minimum bulk volume at 2.6 km^3, which is negligible when compared to that of the ignimbrite. Removing 15 vol.% of xenolithic material from the ignimbrite and the Plinian fall deposit yields bulk volumes of pure juvenile material of 153 km^3 and 2.2 km^3, respectively. Using a density of 2400 $kg \cdot m^{-}$

398 ^{3} for dense rhyolitic material implies a Dense Rock Equivalent (D.R.E.) volume of at least
399 65 km^3 for the magma body that fed the Kızılkaya eruption (the additional volume of the
400 intracaldera fill is unknown). This result is a minimal estimate and we surmise that the total
401 D.R.E. volume is more likely in the range of 70-100 km^3, the eruption of which typically
402 produces collapse structures of 15-20 km in diameter (Geshi et al., 2014).
403
404 *4.4. Shape of the erupted reservoir*
405 Given the extremely homogeneous composition and identical mineralogy of the three
406 samples collected at three different sites, there is no evidence of magma mixing or zoning
407 in the reservoir. The near-Gaussian pressure distribution (Figure 6a) is unlikely to be solely
408 the result of a natural phenomenon. Instead, it can be readily explained by analytical
409 uncertainties of the electron microprobe (which produce a Gaussian distribution) combined
410 with an initial amphibole depth distribution in the magma chamber. Theoretical pressure
411 distributions were modelled for different magma chamber thicknesses by (1) considering
412 amphibole crystals originating at different depths in the eruptible magma body, with a
413 homogeneous repartition with depth, (2) calculating a Gaussian pressure distribution for
414 each crystal, using average pressure and the analytical standard deviation from the
415 microprobe (21 MPa) and (3) summing the resulting pressure distributions for all the
416 crystals (Figure 6a). We then calculated the residual sum of squares between the modelled
417 and the observed pressure distributions, as a function of the magma chamber thickness
418 (Figure 6a). The best fit is obtained for a magma chamber thickness of 1.1 km, equivalent
419 to 30 MPa. When looking at pressure variations instead of absolute pressures, the precision

(2σ) of the barometer is about 21 MPa (0.8 km). The inferred thickness of the erupted fraction of the magma chamber that fed the Kızılkaya eruption is thus 1.1 ± 0.8 km.

The minimum estimated volume for the Kızılkaya ignimbrite and concomitant Plinian tephra fall deposit is 65 km^3 D.R.E. of magma. Considering a sill-like magma body (Figure 6b), with a thickness of 1.1 ± 0.8 km, the estimated diameter of the magma reservoir is 7-17 km. A caldera of larger diameter (at least on the order of 15-20 km) should be expected around the source of the Kızılkaya eruption (Figure 6b), as collapse of the magma chamber's roof involves formation of inclined faults above it, which translate into a wider collapse structure at the surface (Roche et al., 2000). Volcanological (Le Pennec et al., 1994) and geophysical (Froger et al., 1998) investigations in the Cappadocia area have identified two caldera complexes formed by nested collapse structures. One northern collapse structure is about 15 km in diameter, while the southern, more complicated collapsed area is roughly 35 km long by 23 km wide. The size of the southern nested collapse system is consistent with the presence of a caldera similar to that formed above the Kızılkaya magma reservoir, coalescent with other calderas of previous large silicic eruptions from the same system. The range of aspect ratios (thickness over diameter) for the reconstructed Kızılkaya magma reservoir is between 0.02 and 0.3, supporting a pre-eruptive pancake-shaped magma body (Figure 6b). These aspect ratios are in excellent agreement with reservoir shapes inferred from geophysical studies and modelling of other silicic systems worldwide (Bachmann and Bergantz, 2008; Gregg et al., 2012; Wilson, 2001).

5. Application to future large silicic eruptions

Based on the approach above, our new temperature-independent barometer is a promising tool for imaging silicic magma chambers since the silicic products of most large silicic eruptions contain amphibole crystals. Statistical analysis of large amphibole populations is much more accurate than random analyses of a limited number of crystals. This methodology can unfortunately only be used on past eruptions since only full eruption of the magma lenses can provide an image of their crystal cargo. However, many large silicic eruptions are preceded by small volume precursor eruptions (e.g., over 20 ka for the caldera-forming Crater Lake eruption, Bacon and Lanphere, 2006) that can be used to locate the active magma reservoirs and aid in interpretation of geophysical signals. For example, the Laguna del Maule volcanic complex in Chile has been proposed as a developing future large silicic eruption (Feigl et al., 2014; Singer et al., 2014). Small amphibole-bearing rhyodacitic domes have been emplaced in the area over the past 20 ka (Andersen et al., 2017). Using the amphibole compositions published by Andersen et al., (2017), our barometer predicts that these small volumes of magma were initially stored at depths close to 5 km (110-140 MPa, Table 2), with one exception being stored deeper at ~8 km (220 MPa). This value coincides with the deformation source estimated from INSAR data (5.2 ± 0.3 km, Feigl et al., 2014), and is within error of the 200 ± 50 MPa optimal reservoir depth calculated by Huber et al. (2019). The pre-eruptive storage depth of potential small precursor eruptions may thus possibly be indicative of the uppermost part of the growing large silicic reservoir and serve as an indicator for the interpretation of seismological and other geophysical data. Note that those quick calculations are only presented here for illustration purposes, and a full investigation of magma storage depth at Laguna del Maulle is beyond the scope of this study. Also, uncertainties associated with

using literature data might be higher than our stated 72 MPa uncertainty since we do not know the analytical conditions used by Andersen et al. (2017).

dome name	rdcn	Rdcd	Rdne	Rdno	rdac
average pressure (MPa)	127	222	137	126	113
uncertainty, 2σ (MPa)	72	112	72	80	72
average depth (km)	4.8	8.4	5.2	4.8	4.3
uncertainty, 2σ (km)	2.7	4.2	2.7	3.0	2.7
age (ka)	3.5	8.0	>19	>19	20.0
uncertainty (ka)	2.3	0.8			1.2

Table 2. Estimated storage pressures and depths for five recent rhyodacite domes in the Laguna del Maule area, calculated from the analytical data of (Andersen et al., 2017). Depth estimations assume a 2700 $kg \cdot m^{-3}$ density for the granitic crust. Reported ages are $^{40}Ar/^{39}Ar$ ages from Andersen et al. (2017). Uncertainties are reported at the 2σ level as either data dispersion, indicating analytical errors or multiple crystal provenance, or model accuracy (72 MPa = 2.7 km), whichever is higher.

Combination of petrological and volcanological data thus provides refined constraints on the shape of large silicic magma reservoirs and can serve as a guide for geophysical monitoring of future eruptions, particularly in areas where signals suggest the Earth is getting ready for a new large silicic eruption and pre-climactic amphibole-bearing products are emitted (e.g., Heise et al., 2010; Le Mével et al., 2016; Seccia et al., 2011). Further improvement of amphibole barometry, relying on crystal chemistry and thermodynamics rather than empirical correlations, and grounded in high-quality experimental data is desirable in order to better image past and active silicic volcanic systems.

References

Andersen, N.L., Singer, B.S., Jicha, B.R., Beard, B.L., Johnson, C.M., Licciardi, J.M., 2017. Pleistocene to Holocene growth of a large upper crustal rhyolitic magma reservoir beneath the active Laguna del Maule volcanic field, central Chile. Journal of Petrology 58, 85–114.

Aydar, E., Schmitt, A.K., Çubukçu, H.E., Akin, L., Ersoy, E., 2012. Correlation of ignimbrites in the central Anatolian volcanic province using zircon and plagioclase ages and zircon compositions. Journal of Volcanology and Geothermal Research 213-214, 83-97.

Bachmann, O., Bergantz, G., 2008. The magma reservoirs that feed supereruptions. Elements 4, 17–21.

Bachmann, O., Dungan, M.A., 2002. Temperature-induced Al-zoning in hornblendes of the Fish Canyon magma, Colorado. American Mineralogist 87, 1062–1076.

Bacon, C.R., Lanphere, M.A., 2006. Eruptive history and geochronology of Mount Mazama and the Crater Lake region, Oregon. GSA Bulletin 118, 1331–1359.

Clowe, C.A., Popp, R.K., Fritz, S.J., 1988. Experimental investigation of the effect of oxygen fugacity on ferric-ferrous ratios and unit-cell parameters of four natural clinoamphibole. American Mineralogist 73, 487–499.

Feigl, K.L., Le Mével, H., Tabrez Ali, S., Córdova, L., Andersen, N.L., DeMets, C., Singer, B.S., 2014. Rapid uplift in Laguna del Maule volcanic field of the Andean Southern Volcanic zone (Chile) 2007–2012. Geophysical Journal International 196, 885–901.

Froger, J.-L., Lénat, J.-F., Chorowicz, J., Le Pennec, J.-L., Bourdier, J.-L., Köse, O., Zimitoglu, O., Gündogdu, N.M., Gourgaud, A., 1998. Hidden calderas evidenced by multisource geophysical data; example of Cappadocian Calderas, Central Anatolia. Journal of Volcanology and Geothermal Research 85, 99–128.

Geshi, N., Ruch, J., Acocella, V., 2014. Evaluating volumes for magma chambers and magma withdrawn for caldera collapse. Earth and Planetary Science Letters 396, 107–115.

Gregg, P.M., de Silva, S.L., Grosfils, E.B., Parmigiani, J.P., 2012. Catastrophic caldera-forming eruptions: Thermomechanics and implications for eruption triggering and maximum caldera dimensions on Earth. Journal of Volcanology and Geothermal Research 241–242, 1–12.

Hammarstrom, J.M., Zen, E.-A., 1986. Aluminum in hornblende: An empirical igneous geobarometer. American Mineralogist 71, 1297–1313.

Hawthorne, F.C., Oberti, R., Harlow, G.E., Maresch, W.V., Martin, R.F., Schumacher, J.C., Welch, M.D., 2012. Nomenclature of the amphibole supergroup. American Mineralogist 97, 2031–2048.

Heise, W., Caldwell, T.G., Bibby, H.M., Bennie, S.L., 2010. Three-dimensional electrical resistivity image of magma beneath an active continental rift, Taupo Volcanic Zone, New Zealand: melt distribution of Taupo volcanic zone. Geophys. Res. Lett. 37, L10301.

Holland, T., Blundy, J., 1994. Non-ideal interactions in calcic amphiboles and their bearing on amphibole-plagioclase thermometry. Contr. Mineral. and Petrol. 116, 433–447.

529 Hollister, L.S., Grissom, G.C., Peters, E.K., Stowell, H.H., Sisson, V.B., 1987.
530 Confirmation of the empirical correlation of Al in hornblende with pressure of
531 solidification of calc-alkaline plutons. American Mineralogist 72, 231–239.
532 Huber, C., Townsend, M., Degruyter, W., Bachmann, O. (2019) Optimal depth of
533 subvolcanic magma chamber growth controlled by volatiles and crust rheology.
534 Nature Geoscience 12(9): 762-768.
535 Johnson, M.C., Rutherford, M.J., 1989. Experimental calibration of the aluminum-in-
536 hornblende geobarometer with application to Long Valley caldera (California)
537 volcanic rocks. Geology 17, 837–841.
538 Krawczynski, M.J., Grove, T.L., Behrens, H., 2012, Amphibole stability in primitive arc
539 magmas: effects of temperature, H_2O content, and oxygen fugacity. 164: 317-339.
540 Larocque, J., Canil, D., 2010. The role of amphibole in the evolution of arc magmas and
541 crust: the case from the Jurassic Bonanza arc section, Vancouver Island, Canada.
542 Contribution to Mineralogy and Petrology 159: 475-492.
543 Le Mével, H., Gregg, P., Feigl, K.L., 2016. Magma injection into a long-lived reservoir to
544 explain geodetically measured uplift: Application to the 2007-2014 unrest episode
545 at Laguna del Maule volcanic field, Chile. Journal of Geophysical Research 81,
546 6092-6108.
547 Le Pennec, J.-L., Bourdier, J.-L., Froger, J.-L., Temel, A., Camus, G., Gourgaud, A., 1994.
548 Neogene ignimbrites of the Nevsehir plateau (central Turkey): stratigraphy,
549 distribution and source constraints. Journal of Volcanology and Geothermal
550 Research 63, 59–87.
551 Legros, F., 2000. Minimum volume of a tephra fallout deposit estimated from a single
552 isopach. Journal of Volcanology and Geothermal Research 96, 25–32.
553 Lowenstern, J.B., Smith, R.B., Hill, D.P., 2006. Monitoring super-volcanoes: geophysical
554 and geochemical signals at Yellowstone and other large caldera systems. Phil.
555 Trans. R. Soc. A. 364, 2055–2072.
556 Manrique, N., Samaniego, P., Médard, E., Schiavi, F., Mariño, J., Liorzou, C., 2020. Pre-
557 eruptive magmatic processes associated with the historical (218 ± 14 aBP)
558 explosive eruption of Tutupaca volcano (southern Peru). Bull Volcanol 82, 6.
559 Miller, C.F., Wark, D.A., 2008. Supervolcanoes and their explosive supereruptions.
560 Elements 4, 11–15.
561 Mutch, E.J.F., Blundy, J.D., Tattitch, B.C., Cooper, F.J., Brooker, R.A., 2016. An
562 experimental study of amphibole stability in low-pressure granitic magmas and a
563 revised Al-in-hornblende geobarometer. Contribution to Mineralogy and Petrology
564 171, 85.
565 Newhall, C.G., Punongbayan, R., S., 1996. Fire and mud: eruptions and lahars of Mount
566 Pinatubo, Philippines, University of Washington Press. ed., Seattle.
567 Papale, P., Moretti, R., Barbato, D., 2006. The compositional dependence of the saturation
568 surface of $H_2O + CO_2$ fluids in silicate melts. Chemical Geology 229, 78–95.
569 Paquette, J.-L., Le Pennec, J.-L., 2012. 3.8 Ga zircons sampled by Neogene ignimbrite
570 eruptions in Central Anatolia. Geology 40, 239–242.
571 Popa R.-G., Bachmann O., Huber C., 2021. Explosive or effusive style of volcanic eruption
572 determined by magma storage conditions. Nature Geoscience 14(10): 781-786.
573 Pritchard, M., Gregg, P.M., 2016. Geophysical evidence for silicic crustal melt in the
574 continents: where, what kind, and how much? Elements 12, 121–127.

575 Putirka, K.D., 2008. Thermometers and Barometers for Volcanic Systems. Reviews in
576 Mineralogy and Geochemistry 69, 61–120.
577 Putirka, K.D., 2016. Amphibole thermometers and barometers for igneous systems and
578 some implications for eruption mechanisms of felsic magmas at arc volcanoes.
579 American Mineralogist 101: 841-858.
580 Ridolfi, F., Renzulli, A., 2012. Calcic amphiboles in calc-alkaline and alkaline magmas:
581 thermobarometric and chemometric empirical equations valid up to 1,130°C and 2.2
582 GPa. Contrib Mineral Petrol 163, 877–895.
583 Ridolfi, F., Renzulli, A., Puerini, M., 2010. Stability and chemical equilibrium of
584 amphibole in calc-alkaline magmas: an overview, new thermobarometric
585 formulations and application to subduction-related volcanoes. Contrib Mineral
586 Petrol 160, 45–66.
587 Roche, O., Druitt, T.H., Merle, O., 2000. Experimental study of caldera formation. J.
588 Geophys. Res. 105, 395–416.
589 Rondet, M., Martel, C., Bourdier, J.-L., 2019. The intermediate step in fractionation trends
590 of mildly alkaline volcanic suites: An experimental insight from the Pavin
591 trachyandesite (Massif Central, France). Comptes Rendus Geoscience 351, 525–
592 539.
593 Rutherford, M.J., Devine, J.D., 2003. Magmatic conditions and magma ascent as indicated
594 by hornblende phase equilibria and reactions in the 1995±2002 Soufrière Hills
595 magma 44, 1433-1454.
596 Rutter, M.J., Van der Laan, S.R., Wyllie, P.J., 1989. Experimental data for a proposed
597 empirical igneous geobarometer: Aluminum in hornblende at 10 kbar pressure.
598 Geology 17, 897–900.
599 Samaniego, P., Valderrama, P., Mariño, J., van Wyk de Vries, B., Roche, O., Manrique, N.,
600 Chédeville, C., Liorzou, C., Fidel, L., Malnati, J., 12015. The historical (218±14
601 aBP) explosive eruption of Tutupaca volcano (Southern Peru). Bull Volcanol 77,
602 51.
603 Schiavi, F., Bolfan-Casanova, N., Withers, A.C., Médard, E., Laumonier, M., Laporte, D.,
604 Flaherty, T., Gómez-Ulla, A., 2018. Water quantification in silicate glasses by
605 Raman spectroscopy: Correcting for the effects of confocality, density and ferric
606 iron. Chemical Geology 483, 312–331.
607 Schmidt, M.W., 1992. Amphibole composition in tonalite as a function of pressure: an
608 experimental calibration of the Al-in-hornblende barometer. Contribution to
609 Mineralogy and Petrology 110, 304–310.
610 Seccia, D., Chiarabba, C., De Gori, P., Bianchi, I., Hill, D.P., 2011. Evidence for the
611 contemporary magmatic system beneath Long Valley Caldera from local earthquake
612 tomography and receiver function analysis. Journal of Geophysical Research: Solid
613 Earth 116, B12314.
614 Self, S., Blake, S., 2008. Consequences of explosive supereruptions. Elements 4, 41–46.
615 Shane, P., Smith, V.C., 2013. Using amphibole crystals to reconstruct magma storage
616 temperatures and pressures for the post-caldera collapse volcanism at Okataina
617 volcano. Lithos 156–159, 159–170.
618 Singer, B.S., Andersen, N.L., Le Mével, H., Feigl, K.L., DeMets, C., Tikoff, B., Thurber,
619 C.H., Jicha, B.R., Cardona, C., Córdova, L., Gil, F., Unsworth, M.J., Williams-
620 Jones, G., Miller, C.A., Fierstein, J., Hildreth, W., Vasquez, J., 2014. Dynamics of a

large, restless, rhyolitic magma system at Laguna del Maule, southern Andes, Chile. GSA Today 24, 4–10.
Temel, A., Gündogdu, M.N., Gourgaud, A., Le Pennec, J.-L., 1998. Ignimbrites of Cappadocia (Central Anatolia, Turkey): petrology and geochemistry. Journal of Volcanology and Geothermal Research 85, 447–471.
Thomas, W.M., Ernst, W.G., 1990. The aluminum content of hornblende in calc-alkaline granitic rocks: a mineralogic barometer calibrated experimentally to 12 kbars, in: Fluid-Mineral Interactions: A Tribute to H.P. Eugster. pp. 59–63.
Viereck-Goette, L., Lepetit, P., Gürel, A., Ganskow, G., Çopuroğlu, I., Abratis, M., 2010. Revised volcanostratigraphy of the Upper Miocene to Lower Pliocene Ürgüp Formation, Central Anatolian volcanic province, Turkey, in: Stratigraphy and Geology of Volcanic Areas, Geological Society of America Special Paper. pp. 85–112.
Wilson, C.J.N., 2001. The 26.5 ka Oruanui eruption, New Zealand: an introduction and overview. Journal of Volcanology and Geothermal Research 112, 133–174.

Acknowledgements: This research was supported by the MISTRAL/Termex program of CNRS/INSU through the "Volhexan" project. The Tutupaca sample was collected during fieldwork in Peru funded by the Institut de Recherche pour le Développement (IRD) and with help from Pablo Samaniego (IRD) and Marco Rivera (Instituto Geofísico del Perú). Claire Fonquernie and Jean-Louis Paquette helped with the preparation of the Kızılkaya samples. Federica Schiavi helped with the Raman analyses. This manuscript benefited from discussions with Audrey M. Martin, Justine E. Francomme, Pablo Samaniego, Abidin Temel, and Nélida Manrique, as well as constructive reviews by Olivier Bachmann and Jake Lowenstern and editorial handling by Michael Roden. This is Labex Clervolc contribution xxx.

Figure Captions

Figure 1. Total aluminum (a) and octahedral aluminum (^{VI}Al, b) per formula unit as a function of pressure. Pressure uncertainties are smaller than the symbols. Uncertainties for

652 total aluminum are 8 MPa, and for octahedral aluminum close to 36 MPa. Existing
653 calibrations based on total aluminum are plotted for comparison in (a): Johnson and
654 Rutherford (1989), red dashed line; Schmidt (1992), green dashed line; Mutch et al. (2016),
655 black curve. Experimental data are from Johnson and Rutherford (1989), Mutch et al.
656 (2016), Rutter et al. (1989), Schmidt (1992), Thomas and Ernst (1990). In (b), a least-
657 squares linear regression through the data gives a correlation coefficient of 0.939 and a
658 standard error of estimate of 86 MPa (72 MPa for data ≤ 400 MPa).
659
660 **Figure 2.** Microprobe analytical precision for our new barometer based on octahedral
661 aluminum as a function of the product of beam current and counting time. By optimizing
662 analytical conditions, the precision can be decreased to 10-11 MPa (at the 1σ level).
663
664 **Figure 3.** a) SEM image of a zoned amphibole crystal from the Paipatja unit of the 218 ±
665 14 aBP eruption of Tutupaca volcano in Peru (Manrique et al., 2020). B) Calculated
666 pressure profiles using existing temperature-dependent amphibole barometers (Johnson and
667 Rutherford, 1989; Mutch et al., 2016; Ridolfi et al., 2010; Ridolfi and Renzulli, 2012;
668 Rutter et al., 1989; Thomas and Ernst, 1990) and our new pressure-independent barometer.
669 Note that the tentative calibrations of amphibole-melt barometers proposed by Putirka
670 (2016) are not discussed here because melt compositions are mostly not available in our
671 calibration database, and not often available in natural samples. The pressure profile shows
672 a significant step at the core-rim boundaries for all previously published barometers. This
673 step is an artefact linked to the increase in temperature (Bachmann and Dungan, 2002;
674 Rutherford and Devine, 2003; Shane and Smith, 2013). The grey area represents the

675 average and 2σ standard deviation of our data. Temperature on the right indicate the
676 average experimental temperature in the calibration database for each model.
677
678 **Figure 4.** Calculated crystallization pressure for the core of the investigated amphibole
679 crystal from the Paipatja unit of the 218 ± 14 aBP eruption of Tutupaca volcano in Peru
680 (Manrique et al., 2020) using published barometers as a function of the average calibration
681 temperature of the barometer. There is a very good correlation between calibration
682 temperature and calculated pressure, except for one barometer (Thomas and Ernst, 1990).
683 The white circle represents the pressure estimated with our barometer and the estimated
684 temperature of the crystal core (Manrique et al., 2020).
685
686 **Figure 5.** Calculated crystallization pressure as a function of experimental pressure for a
687 series of experiments containing amphibole and plagioclase. Experiments from the
688 calibration database contain amphibole, plagioclase, biotite, sanidine and quartz (or very
689 close to saturation with sanidine and quartz, Johnson and Rutherford (1989), Mutch et al.
690 (2016), Rutter et al. (1989), Schmidt (1992), Thomas and Ernst (1990)). Samples from
691 Rondet et al. (2019) still contain amphibole, plagioclase and biotite, but are far from
692 saturation with sanidine and quartz (trachy-andesitic composition). Experiments from First
693 et al. (2021) were run on a dacitic composition and contain amphibole and plagioclase with
694 (green circles with black rim) and without (green circles with green rim) biotite. Our new
695 barometer reproduces well experimental pressure for samples containing at least
696 amphibole, plagioclase and biotite.
697

Figure 6. a) Pressure distribution for the 188 investigated amphibole crystals. The distribution is close to a Gaussian one, with an average value of 214 MPa and a 1σ standard deviation of 18 MPa. Also plotted are modelled pressure distributions calculated for various magma chamber equivalent thicknesses: 60 MPa (flat top curve); 30 MPa (best fit to the data, solid line); and 0 MPa (theoretical infinitely flat chamber). The inset shows the residual sum of squares between modelled and observed pressure distributions as a function of magma chamber equivalent thickness. The data are fitted by a fourth-order polynomial with a minimum value at ~30 MPa. b) Reconstructed pre-eruptive shape of the magma chamber and post-eruptive feature, together with a schematic interpretation of magma reservoirs (redrawn from Bachmann and Bergantz, 2008).

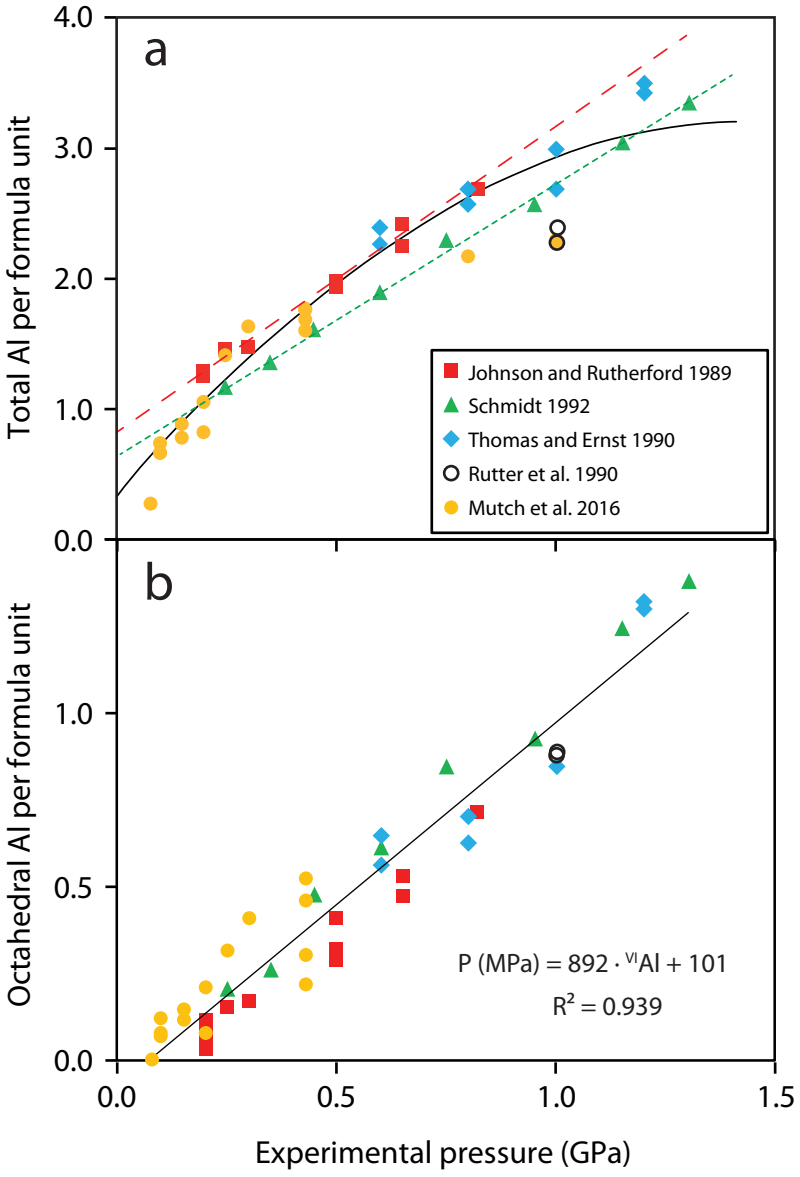
a
b
Total Al per formula unit
Octahedral Al per formula unit
Experimental pressure (GPa)
Johnson and Rutherford 1989
Schmidt 1992
Thomas and Ernst 1990
Rutter et al. 1990
Mutch et al. 2016
P (MPa) = 892 · VIAl + 101
R2 = 0.939
4.0
3.0
2.0
1.0
0.0
0.5
1.5

Figure 1

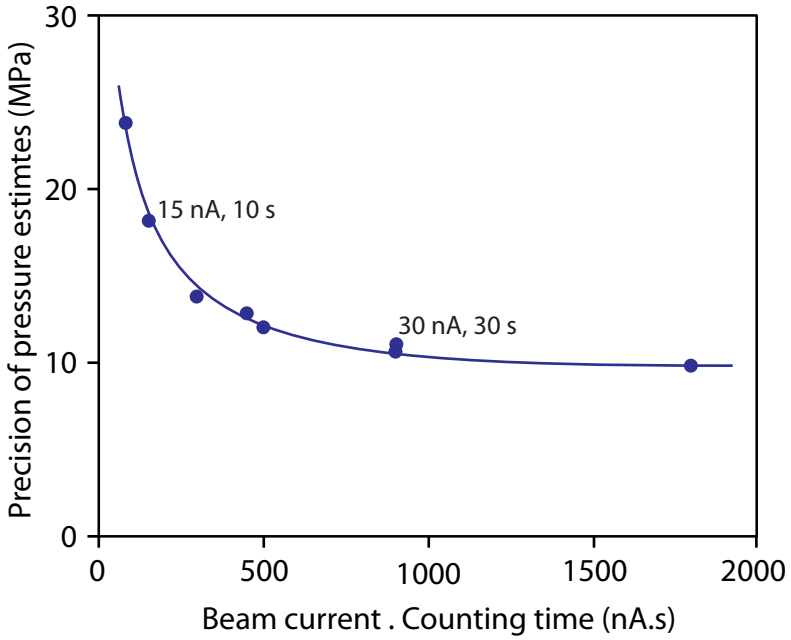
30
20
10
0
Precision of pressure estimtes (MPa)
15 nA, 10 s
30 nA, 30 s
0
500
1000
1500
2000
Beam current . Counting time (nA.s)

Figure 2

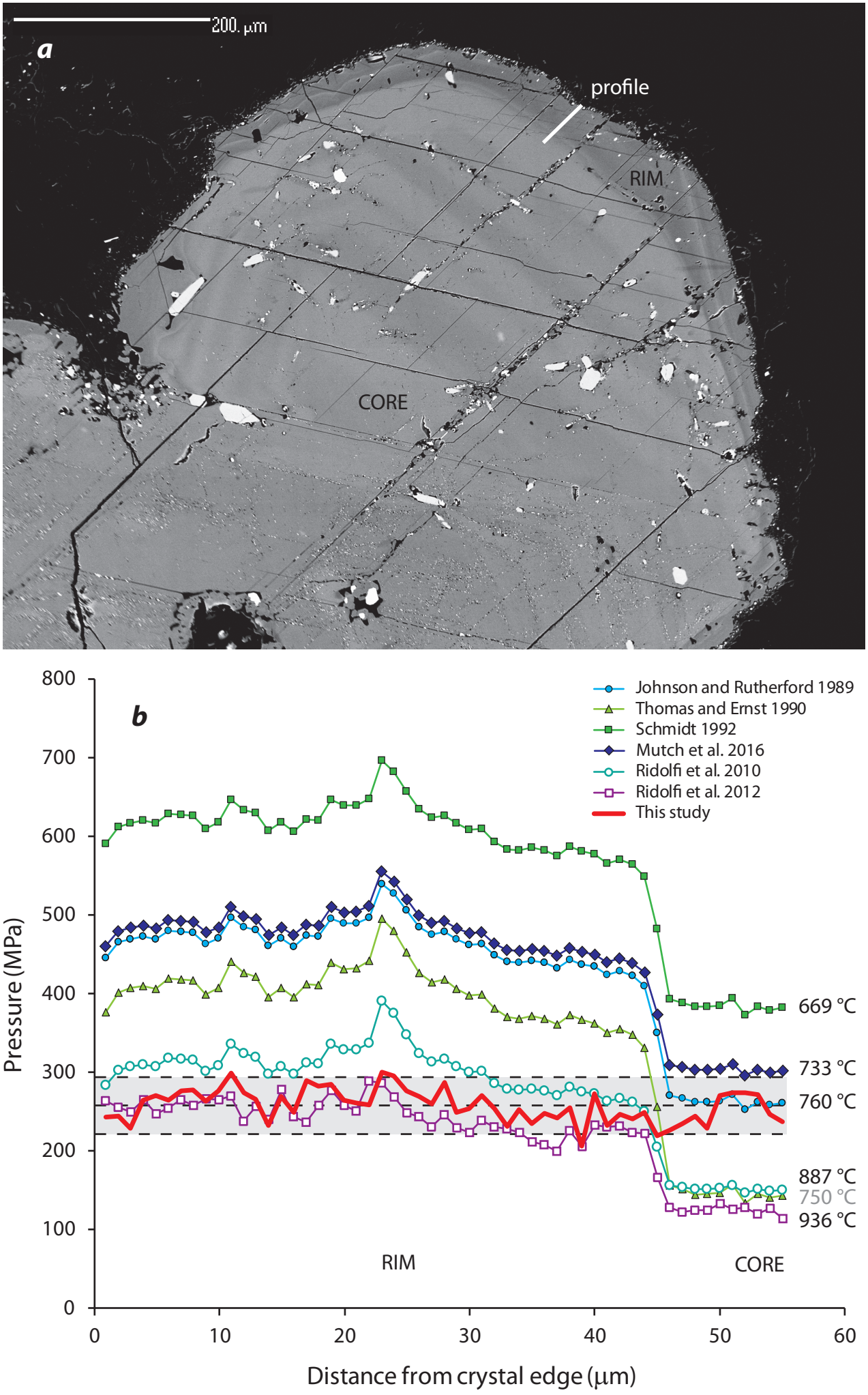
a
200. µm
profile
RIM
CORE
b
Johnson and Rutherford 1989
Thomas and Ernst 1990
Schmidt 1992
Mutch et al. 2016
Ridolfi et al. 2010
Ridolfi et al. 2012
This study
669 °C
733 °C
760 °C
887 °C
750 °C
936 °C
RIM
CORE
Pressure (MPa)
Distance from crystal edge (µm)
0
100
200
300
400
500
600
700
800
0
10
20
30
40
50
60

Figure 3

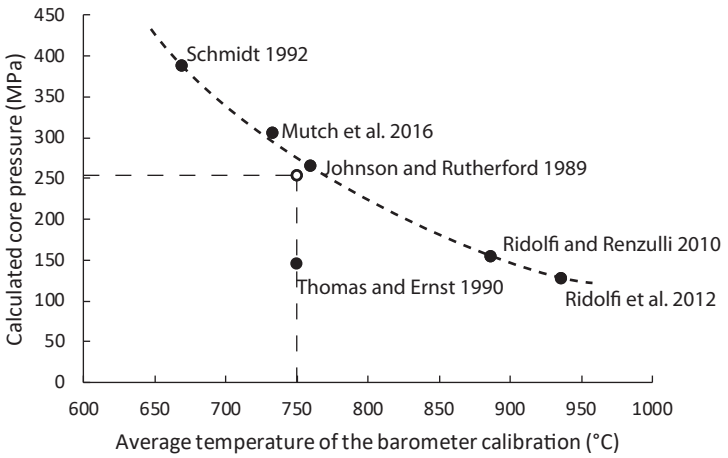
Calculated core pressure (MPa)
450
400
350
300
250
200
150
100
50
0
600
650
700
750
800
850
900
950
1000
Average temperature of the barometer calibration (°C)
Schmidt 1992
Mutch et al. 2016
Johnson and Rutherford 1989
Ridolfi and Renzulli 2010
Thomas and Ernst 1990
Ridolfi et al. 2012

Figure 4

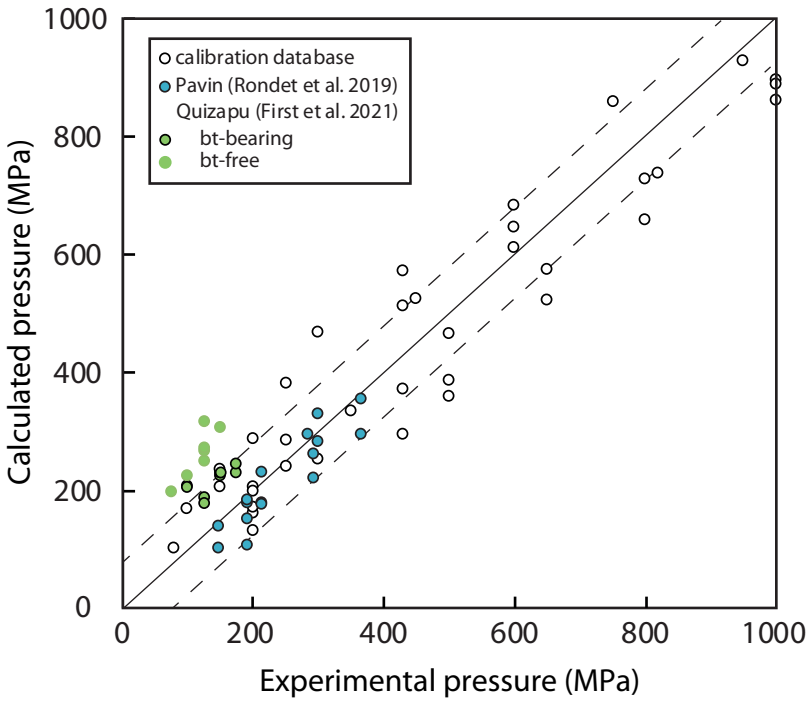
calibration database
Pavin (Rondet et al. 2019)
Quizapu (First et al. 2021)
bt-bearing
bt-free
Calculated pressure (MPa)
Experimental pressure (MPa)
0
200
400
600
800
1000

Figure 5

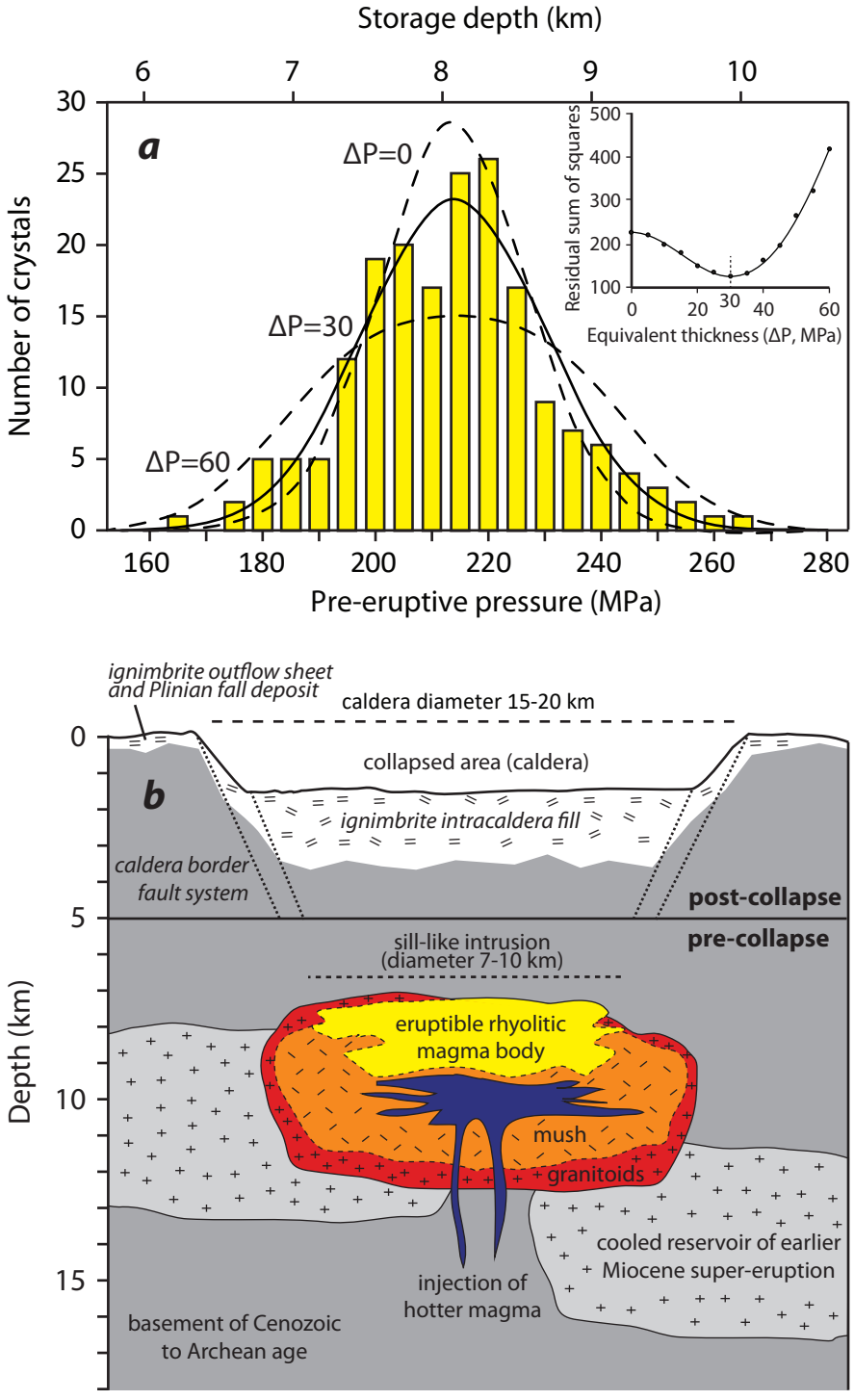
Storage depth (km)
6
7
8
9
10
a
ΔP=0
ΔP=30
ΔP=60
Number of crystals
Pre-eruptive pressure (MPa)
Residual sum of squares
Equivalent thickness (ΔP, MPa)
ignimbrite outflow sheet and Plinian fall deposit
caldera diameter 15-20 km
collapsed area (caldera)
b
ignimbrite intracaldera fill
caldera border fault system
post-collapse
pre-collapse
sill-like intrusion (diameter 7-10 km)
eruptible rhyolitic magma body
mush
granitoids
cooled reservoir of earlier Miocene super-eruption
injection of hotter magma
basement of Cenozoic to Archean age
Depth (km)

Figure 6